Advancements, measurement uncertainties, and recent comparisons of the NOAA frostpoint hygrometer

Emrys G. Hall[1,2], Allen F. Jordan[1,2], Dale F. Hurst[1,2], Samuel J. Oltmans[2], Holger Vömel[3], Benjamin Kühnreich[4,5], Volker Ebert[4,5]

[1]Cooperative Institute for Research in Environmental Sciences, University of Colorado, Boulder, Colorado, USA
[2]NOAA Earth System Research Laboratory, Global Monitoring Division, Boulder, Colorado, USA
[3]National Center for Atmospheric Research, Earth Observation Laboratory, Boulder, Colorado, USA
[4]Physikalisch-Technische Bundesanstalt, Braunschweig, Germany
[5]Center of Smart Interfaces, Technische Universität Darmstadt, Germany

Correspondence to: Emrys G. Hall (Emrys.Hall@noaa.gov)

Abstract. The NOAA frostpoint hygrometer (FPH) is a balloon borne instrument flown monthly at three sites to measure water vapor profiles up to 28 km. The FPH record from Boulder, Colorado is the longest continuous stratospheric water vapor record. The instrument has an uncertainty in the stratosphere that is < 6 % and up to 12 % in the troposphere. A digital microcontroller version of the instrument improved upon the older versions in 2008 with sunlight filtering, better frost control, and resistance to radio frequency interference (RFI). A new thermistor calibration technique was implemented in 2014, decreasing the uncertainty in the thermistor calibration fit to less than 0.01 °C over the full range of frostpoint temperatures (-93 °C to +20 °C) measured during a profile. Results from multiple water vapor intercomparisons are presented, including the excellent agreement during AquaVIT-2 chamber experiments over six days that provides confidence in the accuracy of the FPH measurements. Dual instrument flights with two FPHs or an FPH and a cryogenic frostpoint hygrometer (CFH) also show good agreement when launched on the same balloon. The results from these comparisons demonstrate the high level of accuracy of the NOAA FPH.

1 Introduction

Water vapor is the most abundant and important greenhouse gas in the atmosphere and contributes to many processes and feedback mechanisms. Though the vast majority of this highly variable invisible gas is found near the surface, water vapor in the upper troposphere and stratosphere can significantly influence climate.

The concentration of water vapor in the stratosphere is controlled by transport through the tropical tropopause layer (TTL) rendering the stratospheric air extremely dry through a freeze drying process (Brewer, 1949). The seasonal cycle of the tropical tropopause temperature controls the seasonal cycle of water vapor entering the stratosphere which is advected upward and poleward (Mote et al., 1996). Methane oxidation is a photochemical source of water vapor in the atmosphere but can only account for 25–34 % of the net stratospheric water vapor increase between 1978 to 2003 (Rohs et al., 2006). Water

vapor plays a role in cirrus cloud formation which impacts Earth's radiation budget. High thin cirrus clouds may cool the surface while producing a net warming in the stratosphere by absorbing outgoing longwave radiation in the atmosphere (Lee et al., 2009).

The Boulder stratospheric water vapor record shows a net increase of ~1 ppmv (27 %) since 1980 (Hurst et al., 2011a) with a

5 sharp decrease of roughly 10 % in 2001 to 2005 (Randel et al., 2006; Rosenlof and Reid, 2008). Solomon et al. (2010) estimated that this sharp drop in stratospheric water vapor in 2001 decelerated the global surface temperature increase by approximately 25 % compared to what would have been caused by well-mixed greenhouse gases between 2000 and 2009. It is imperative to monitor the distribution of water vapor especially in the stratosphere where it represents an important driver of decadal world-wide surface climate change (Solomon et al., 2010).

10 Accurate measurements of upper tropospheric and lower stratospheric (UTLS) water vapor are pivotal for understanding changes in stratospheric water vapor and their impact on the radiative forcing (Foster and Shine, 2002) of our climate. Worldwide there are more than 800 radiosonde stations launching balloon instruments twice daily totaling > 500,000 vertical profiles of wind speed/direction, pressure, temperature, and humidity each year. These measurements are predominately used for weather forecasting. While radiosonde wind, pressure, and temperature measurements are accurate up to balloon burst (>

15 30 km), the relative humidity measurements often lack the precision and accuracy necessary for climate research and are most useful in the low to mid troposphere. Stratospheric water vapor is deceptively hard to measure, despite the relatively high concentration (> 1 ppmv) compared to most trace gases in the atmosphere. Vertical profiles of UTLS water vapor have been measured by satellite, aircraft, lidar, and balloon borne instruments revealing considerable disagreements (~25–100 %) between a core group of stratospheric water vapor measurements (Kley et al., 2000; Weinstock et al., 2009). A 2011

20 intercomparison of two frostpoint hygrometers and five in-situ aircraft hygrometers show reduced but still statistically significant differences of 0.4–0.8 ppmv (10–20 %) (Rollins et al., 2014). Future laboratory and airborne intercomparisons are necessary to further understand the differences while helping to identify errors in calibration and measurement techniques.

The NOAA frostpoint hygrometer (FPH) captures monthly water vapor profiles from three sites around the globe. The longest continuous record of upper atmospheric water vapor abundance began in Boulder, Colorado in 1980. The second site

25 was Lauder, New Zealand which started monthly soundings in 2004. Hilo, Hawaii initiated soundings in late 2010. These three sites were chosen to represent the northern and southern mid latitudes and the tropics, respectively. The typical instrument package flown at these three sites consists of a NOAA FPH, an electrochemical concentration cell (ECC) ozonesonde, and a radiosonde which wirelessly transmits the data back to the receiving station on the ground.

In-situ balloon flight profiles complement satellite sensors monitoring the global distribution of water vapor around the

30 planet. Monthly NOAA FPH balloon measurements provide high vertical resolution profiles. Satellite sensors, such as the Aura Microwave Limb Sounder (MLS) (Read et al., 2007), measure water vapor in the UTLS and above (Lambert et al.,

2007) with almost daily global frequency but with a vertical resolution of 2–3 km. Combining the data from these two measurement techniques provides important distribution information of water vapor for models, to help detect trends, and identify future changes in climate. Differences between the NOAA FPH and the MLS have been explored in depth by Hurst et al. (2014) showing good agreement in the stratosphere (68 to 26 hPa) at all three NOAA Global Monitoring Division

5 (GMD) sites between August 2004 and December 2012. Previous coincident cryogenic frostpoint hygrometer (CFH) balloon observations were used in the validation of the earlier versions of the MLS satellite (v1.5 and v2.2) between 2005 and 2007 (Vömel et al., 2007c). Vömel et al. (2007c) found that MLS and CFH profiles agreed to within 2.7 ± 8.7 % from 68 to 22 hPa. The CFH is a small balloon borne hygrometer developed in 2003 which uses the same fundamental measurement principle as the NOAA FPH (Vömel et al., 2007a). The two instruments have many similarities but also differ in subtle ways

10 including electronics, sunlight filtering, and frost control algorithm.

This paper provides detailed information regarding the description and uncertainty of the current digital FPH along with a brief history of the evolution of the sonde. Comparisons in the laboratory along with dual instrument balloon flights are presented.

2 Instrument description and history

15 The NOAA FPH is an in-situ balloon borne chilled mirror hygrometer capable of measuring vertical profiles of frostpoint temperature up to ~28 km. The basic measurement principle and calibration method have remained unchanged throughout the time series although significant modernization of the instrument occurred over the ongoing 36 year record (Mastenbrook and Oltmans, 1983; Oltmans, 1985; Vömel et al., 1995; Oltmans and Hofmann, 1995; Hurst et al., 2011a). The chilled mirror principle relies on maintaining a thin, stable layer of condensate on a mirror disk through rapid feedback control. A copper

20 cold finger immersed in a dewar containing liquid cryogen provides cooling power throughout the profile (Fig. 1). A polished mirror disk resides at the opposite end of the cold finger with ambient air passing over it at 3 to 6 m s^{-1}. A nichrome heater wrapped around the narrow shaft of the continuous cold finger and mirror piece provides heat to the mirror. An optical source and detector, composed of an infrared light emitting diode (LED) and a photodiode, is used to monitor the mirror's reflectivity as condensate accumulates in the form of dew or frost. A biconvex lens focuses the light returned off the

25 mirror into the photodiode. A calibrated thermistor embedded in the mirror accurately measures the frostpoint temperature. The frostpoint temperature is achieved when a stable frost layer is present, showing equilibrium between water vapor in the air sample and the condensate on the mirror. Due to the material and geometry, the surface of the mirror is considered to be uniform in temperature across the 7.1 mm diameter (Mastenbrook and Oltmans, 1983). The Goff Gratch formulation of the Clausius-Clapeyron equation (Goff and Gratch, 1946; Goff, 1957) is used to calculate the water vapor partial pressure with

30 respect to ice. Dividing the water vapor partial pressure by the dry atmospheric pressure determines the mixing ratio by volume. The chilled mirror principle is unique in that only the thermistor needs to be calibrated against National Institute of

Standards and Technology (NIST) traceable temperature standards. This eliminates water vapor calibration scales or standards which are difficult to create, maintain, and use in the field.

The NOAA FPH is flown as a disposable instrument that can be reused if returned. The typical instrument package, including an ozonesonde, radiosonde, and liquid cryogen is light-weight (< 1.9 kg) and typically flown using a 1200 g latex

5 balloon. Trifluoromethane (CHF3, R23) has been used as the liquid cryogen since the mid 1990's when the switch was made away from CClF3 (R13). Both compounds have ideal physical properties over a wide range of temperatures (-100 °C to 30 °C) and pressure (10 to 1050 hPa) to provide liquid cooling of the cold finger in all conditions encountered during balloon flights.

The flight train consists of a balloon with a valve in its neck and a parachute attached to a long string unwinder (30–50 m).

10 Nearly all NOAA FPH instrument packages continue to be flown with a valve in the neck of the balloon allowing slow controlled descent profiles to be acquired (Mastenbrook, 1966; Kräuchi et al., 2016). The instrument package resides at the bottom of the unwinder that separates the balloon and parachute from the instrumentation in an effort to reduce water vapor contamination, from balloon outgassing during the ascent.

Over the 36 years of FPH measurements by NOAA, four versions of the instrument have been flown with each change

15 reflecting advancements in the capabilities of the instrument (Table 1). However, each version adhered to the same NIST-traceable temperature calibration standard.

2.1 FPH V1: Analog hygrometer

Balloon borne frostpoint hygrometers have been used to collect vertical profiles of water vapor abundance and distribution in the atmosphere since the late 1950's (Mastenbrook and Dinger, 1961). Monthly profiles were acquired in Washington, DC

20 between 1964 and 1980 using a 4.5 kg balloon borne frostpoint hygrometer specifically developed for the program. The water vapor program was moved to Boulder, Colorado in 1980 following significant instrument improvements that included implementation of solid state electronics (Mastenbrook and Oltmans, 1983). A 1680 MHz VIZ "A" radiosonde telemetered data wirelessly and recorded the data on a paper strip chart. The VIZ "A" radiosonde transmitter was flown 10 feet above the rest of the instrument package to avoid RFI (Mastenbrook, 1981).

25 ### 2.2 FPH V2: Digital interface to Vaisala RS-80 radiosonde

In February 1991, a digital interface was added utilizing a 403 MHz Vaisala RS-80 radiosonde and a separate 8 bit analog to digital converter (ADC) board which was replaced in October 1991 by a 12 bit ADC board. No shifts were detected in the data recorded digitally instead of on the strip chart recorder formerly used with the 1680 MHz VIZ "A" radiosonde (Oltmans et al., 2000). Starting in 1993, several steps were taken to minimize problematic 403 MHz RFI including adding a 1 m

30 horizontal foam boom to separate the radiosonde from the other instrumentation, and adding ferrite beads to any wires on the

FPH. Silver mirrors used before 1977 were replaced with rhodium plated copper mirrors on the Boulder instrument until nickel and gold plated copper mirrors became the standard late in 1992. In 1998 the custom-made aneroid barometer incorporated on the FPH became obsolete forcing replacement by a solid state sensor in the new supporting electronics designed in 2000 and improved upon in 2001.

2.3 FPH V3: Light-weight hygrometer with upgraded electronics

In 2004, a modern electronics board was added utilizing surface mount components that eliminated RFI from the attached radiosonde. Modified mechanical and optical parts were combined with new foam packaging to create an analog FPH boasting a 70 % reduction in weight. These improvements enabled the second NOAA/GMD stratospheric water vapor station to be started at Lauder, New Zealand in 2004.

Prior to the 2004 version of the hygrometer the optical system consisted of two pairs of optical elements in close thermal proximity. The "specular pair" looked down at the mirror through a lens and provided a current proportional to the light reflected off the mirror while the "bias" pair looked directly at each other. The two pairs were matched according to their temperature coefficients and attached to the optics block with thermal epoxy to minimize temperature-driven signal drift in the differential measurement. Before flight, the bias signal was set at 21 % by adjusting a setscrew to match the specular signal setpoint. With the introduction of temperature stabilization of the aluminum optics block the bias pair was deemed unnecessary on all FPH instruments flown after 2004 allowing a fixed resistor to replace the bias pair on the electronics boards.

2.4 FPH V4: Digital microcontroller hygrometer

Between 2005 and 2008, a digital version of the hygrometer was developed that offered greater precision, and ease of use while decreasing the weight, cost, power consumption, and manufacturing time. The skill required to successfully launch and collect water vapor data with the FPH V4 is equivalent to that needed to prepare and release an ozonesonde with an attached radiosonde, of which there are approximately 3000 flown each year by different research groups around the world. The older analog instrument required more in-depth knowledge and time to successfully produce a high quality water vapor profile.

A major advancement to the digital FPH was the introduction of the modulating filter that removes unwanted sunlight from the photodiode signal during a daytime balloon flight, similar to the CFH's earlier implementation (Vömel, 2007a). Earlier versions of the FPH utilized a stainless steel sunshield to block the sunlight except for flights done between 1997 and 2003. The sunshield was effective at blocking sunlight but often contributed to stratospheric contamination on the ascent portion of the flight. The new switching sunlight filter provides clean stratospheric frost control by reducing contamination. Since 2010, the FPH LED is modulated at 24 Hz while the photodiode continually measures the signal from the mirror. The microcontroller calculates the difference between the LED on and off signals in real time during the flight. This enables the

sunlight captured by the photodiode during the LED off periods to be removed from the LED on signal to maintain unvarying condensate coverage during a flight.

Eliminating the sunshield, incorporating a lens heater, and implementing a flexible frostpoint-dependent gain schedule (Vömel, 2007a) were significant improvements linked with the digital FPH. A digital calibrated pressure sensor was
5 incorporated into the hygrometer adding the flexibility to perform tasks throughout the flight based on pressure.

Prior to 2008 the LED in the analog version of the FPH had a wide viewing angle and a peak wavelength centered at 940 nm. This LED and the photodiode were replaced with an 880 nm-peak LED and a 900 nm-centered photodiode, both with narrow viewing angles. Peak wavelength matching is not necessary because the spectral bandwidth at half power is ± 40 nm providing ample overlap. The optics block is temperature controlled to 32.00 ± 0.01 °C throughout the balloon flight. Great
10 care is taken to maintain temperature stability of the photodiode and LED because both are highly temperature sensitive. Since 2009, a lens heater similar to that flown on the CFH (Vömel, 2007a) was implemented to help reduce condensation, which may form on the lens in humid conditions.

The FPH is insulated by several pieces of foam, with a 300 ml foam Dewar on one side of the instrument and a foam battery enclosure housing the optics block, electronics board, and battery pack on the opposite side. Very thin, hydrophobic stainless
15 steel inlet tubes with a diameter of 2.25 cm are glued above and below the sensor housing to deliver clean air across the polished mirror disk in the middle of the sensor housing.

2.4.1 Mirror feedback controller, electronics, and battery power

The FPH uses a custom-made electronics board with an on-board pressure sensor and an 8-bit Atmel AVR microcontroller. The electronics remain between 20–30 °C during a flight by capturing heat from the nearby optics block and batteries. The
20 FPH is powered by a 9 V battery pack with 3.5 Ah capacity. A nichrome heater wrapped around the mirror allows for a maximum heating power of 22 W, more than sufficient to measure dew or frostpoint temperatures anywhere on earth when R23 cryogen is used for cooling.

A 16 bit ADC converter, oversampled to 19 bit, provides continuous mirror reflectivity feedback to the microcontroller from the photodiode. A dynamic schedule of proportional-integral-derivative (PID) gain values, based on a slow moving average
25 of the measured frostpoint temperature, enhances the ability of the FPH to control the frost layer over an extremely wide range (> 10^5) of water vapor number densities in the atmosphere. The modern gain schedule was developed to allow the instrument to be flown anywhere in the world using the same PID gain table.

The older analog version of the NOAA FPH utilized a simple proportional controller with one gain change within a profile. It was not uncommon for the analog instrument to experience frost control oscillations in the first few kilometers of the

profile and directly after the gain change that historically occurred in the middle troposphere. The digital instrument, with the dynamic gain schedule, provides nearly uninterrupted water vapor profile measurements that are used to determine integrated precipitable water (IPW) columns.

Under stable conditions the FPH controls dew or ice on the mirror such that 79.1 % of the light that would reflect off a bare mirror reaches the photodiode. This value has remained constant since 1980. Laboratory testing has shown that increasing the setpoint value by > 7 % doesn't affect the frostpoint temperature measured by the instrument (Fig. 2). Maintaining a constant condensate layer is much more important than the actual setpoint value used.

2.4.2 Radiosonde telemetry and data collection

The FPH has been flown with the InterMet Systems iMet-1-RSB radiosonde since summer 2009 because the previously used Vaisala RS-80 radiosonde became obsolete. This radiosonde provides measurements of pressure, temperature, and humidity (PTU, Hurst et al., 2011b) along with any externally connected instrument data. The iMet-1-RSB supplies GPS location information that enables payload tracking as well as the calculation of wind speed and direction.

The iMet-1-RSB transmits 1 Hz wireless data at 1200 baud allowing up to 120 bytes of data to be sent each second. The iMet-1-RSB radiosonde employs an open source telemetry protocol (XDATA) that allows multiple instruments to be connected via serial daisy chain. Roughly 80 bytes of externally connected instrument data can be sent down along with the PTU and GPS data of the radiosonde. The data are recorded on the ground by a custom-made software program "SkySonde" that was designed and written by NOAA/GMD engineers to receive and demodulate telemetered data from the iMet-1-RSB.

3 Thermistor calibration

Although the equipment used to calibrate thermistors has changed over the years, the thermistor calibration method has remained unchanged, providing greater stability in the absolute calibration of FPHs over the decades. Details regarding the different data acquisition systems, curve fitting routines, and NIST-traceable thermometers are discussed below.

The frostpoint temperature is measured by a bead thermistor embedded in the mirror disk. Each thermistor is individually calibrated in small batches in a 4 L insulated dewar containing pure ethanol. A laboratory stirrer uniformly maintains the alcohol bath temperature during the calibration. The bath temperature is measured with a NIST-traceable thermometer. The thermistors are inserted approximately 16 cm into the alcohol bath and are attached to a digital multimeter outside of the dewar. Between 1980 and 2013, finely ground dry ice chips were manually added to the bath to cool and maintain the alcohol temperature at three targets: 0, -45, and -79 °C. Great care was taken while adding small amounts of dry ice to maintain a ± 0.005 °C tolerance around each of the three setpoints to minimize curve fitting errors. Calibration coefficients were calculated from the measured resistances at the three target temperatures and used in an equation to calculate mirror

temperature during a flight (Clark, 1961). Starting in 2014, calibrations were done by continuously measuring the bath temperature and the resistance of each thermistor as the alcohol bath slowly warmed from -93 °C to +19 °C. The new continuous resistance measurement technique utilizes a 6-point fit instead of the historic 3-point fit eliminating the extrapolation curve fitting correction necessary for the older 3-point fit (see Sect. 3.1 below).

5   A NIST-traceable Hewlett Packard quartz thermometer was employed as the temperature reference between 1980 and 1998. This probe had accuracies of ± 0.075 °C between -80 °C and -50 °C and ± 0.040 °C between -50 °C and +150 °C with a resolution of 0.001 °C over the full range. When the quartz thermometer broke in 1998 a platinum resistance thermometer (PRT, Hart Scientific, USA) became the temperature reference for all calibrations after 1998. This probe has a stated accuracy of ± 0.01 °C with 0.001 °C resolution over the full range of NOAA FPH thermistor calibrations. The Hart PRT

10   probe has been recalibrated by the manufacturer every six years since 1998 and still serves as the NIST-traceable standard today.

Until late 1998 the resistance of each thermistor was hand recorded from an HP digital multimeter. Then a new data acquisition system was developed using a Campbell Scientific CR10 data logger that allowed 20 thermistors to be calibrated at once. During the summer of 2004 an Agilent 34970A data acquisition switching unit was setup as the new primary

15   calibration system, allowing 40 thermistors to be calibrated at a time.

3.1 3-Point thermistor extrapolation correction below -79 °C frostpoint temperature: 1980–2013

The traditional 3-point thermistor curve fit was utilized for thermistor calibrations performed from 1980 to 2013. Between 0 °C and -79 °C the curve fit was better than ± 0.06 °C (Fig. 3). Colder than -79 °C there existed a one-sided extrapolation error with a maximum error of 0.16 °C at -90 °C. Based on a batch of six thermistors calibrated down to -93.3 °C, a linear

20   correction Eq. (1) was applied to frostpoint temperatures colder than -79 °C for all NOAA FPH flights prior to 1991 (Mastenbrook, 1981)

$$T_{FpT,corr} = 1.013(T_{FpT}) + 1.046 \qquad (1)$$

where T_{FpT} is in °C. Scherer et al. (2008) developed an improved empirical fit to correct frostpoint temperatures below -79 °C for all flights between 1991 and the last 3-point thermistor calibration in 2013. The correction was based on the 30

25   thermistor calibration from -100 °C to 20 °C (Vömel et al., 2007b).

$$T_{FpT,corr} = T_{FpT} - (-0.029(T_{FpT} + 79) + 0.083)^2 \qquad (2).$$

Both corrections slightly lowered frostpoint temperatures < -79 °C and reduced water vapor mixing ratios < 3 % in the stratosphere. After the Scherer et al. (2008) correction was applied the calibration curve fits between 1991 and 2013 were better than ± 0.06 °C over the full temperature range.

No corrections were applied to the frostpoint temperatures > 0 °C for any of the FPH data over this period as they would be
5   much smaller than the uncertainties of the FPH measurements in the lower troposphere.

3.2 Thermistor self-heating correction applied to FPH instruments calibrated before 1987

Prior to 1987, all thermistor calibrations were performed using an HP3490A multimeter that applied a known current to each thermistor and determined its resistance by measuring the voltage drop. For resistances < 10 kΩ, the meter applies an excitation current of 0.85 mA that is large enough to heat the small FPH thermistors by ∼ 1.5 °C at the 0 °C calibration point.
10   Calibrations performed after 1987 used a different multimeter with a 0.1 mA excitation current, reducing the self-heating. The self-heating at the two colder calibration points was minimal because both old and new multimeters applied smaller excitation currents.

The self-heating problem at the 0 °C setpoint was documented during a calibration in 1987. A group of 6 thermistors was calibrated using the original 0.85 mA excitation current and the lower 0.1 mA setting. When using the 3-point calibration fit
15   the warm bias at 0 °C produces a cold bias of < 0.21 °C at frostpoint temperatures of -90 °C (Scherer et al., 2008). Utilizing this data, Scherer et. al. (2008) derived an empirical correction that was applied to FPH frostpoint temperatures < -79 °C for all flights before 1987,

$$T_{FpT,corr} = T_{FpT} + (0.0203(T_{FpT} + 61.9))^2 - 0.119 \qquad (3).$$

Applying the empirical correction increases water vapor mixing ratios by < 4 % at -90 °C. All data published since 2008
20   have these two corrections applied where applicable.

3.3 6-Point thermistor calibration: 2014 to present

In 2014 a new calibration technique was implemented. Instead of manually maintaining the calibration bath at 0, -45, and -79 °C, the bath is initially cooled to -93 °C with liquid nitrogen and allowed to slowly warm (Vömel, 2007a), eliminating the need to extrapolate below -79 °C. An expanded version of the Steinhart-Hart formulation now derives fifth order polynomial
25   fits of thermistor resistances to mirror temperature (Steinhart and Hart, 1968) at six calibration temperatures: -91, -80, -59, -39, -15, and +19 °C. These temperatures were selected to minimize fit errors, with greater weighting for the important stratospheric temperature range. The NIST-traceable thermometer temperatures and the resistance values for all 40 channels are recorded continuously on an Agilent 34970A digital multimeter until the bath reached > 19 °C, a process that takes ∼50

hours because the Dewar is well insulated. The probe temperature is measured before and after the two second sweep (< 0.003 °C temperature change during each sweep) of each thermistor and then interpolated to determine the probe temperature during each of the 40 thermistor measurements. The new 6-point fit reduces errors over the full range to better than ± 0.01 °C compared to ± 0.06 °C for the historical 3-point fit (Fig. 3). The discontinuity near -70 °C is caused by the

5   custom data acquisition software switching between the 1 MΩ and the 100 kΩ range setting on the Agilent 34970A digital multimeter in order to measure the lower thermistor resistances as the bath warms. The discontinuity does not affect the balloon flight data as there are no calibration points near -70 °C and the mirror thermistor is measured with the onboard ADC which does not have this issue.

Though far more comprehensive, the new continuous-measurement calibration technique has a complication due to the

10   changing temperature of the bath as it warms. The PRT probe has a larger thermal mass than the thermistors and therefore warms at a slower rate. At each sampling time, the measured probe temperature will be slightly colder than the true temperature of the thermistors. To account for this thermal "lag" a small correction is required.

The thermal lag correction was determined by performing both a historical 3-point calibration and a new continuous-measurement calibration on the same set of thermistors. At the three historical static temperature setpoints there is no

15   thermal lag of the PRT probe despite its larger thermal mass by holding the bath in equilibrium for an extended time at each temperature (> 3 minutes). The results are compared to those from the new continuous-measurement calibration to determine the thermal lag correction for the probe. The correction is dependent on the warming rate of the bath, so an equation is created mapping warming rate to temperature lag correction for use in future calibrations (which may warm at different rates due to varying lab conditions and equipment). Before applying the lag correction, a line is fit to the calculated warming rate

20   to avoid inserting extra noise into the corrected probe temperature data (Fig. 4).

4 Measurement uncertainty

Errors and uncertainties are treated as outlined in the "Guide to the expression of uncertainty in measurement" by the working group 1 of the Joint Committee for Guides in Metrology (JCGM/WG 1, 2008). Uncertainty in the FPH measurements is determined through the evaluation of random and systematic errors. Uncontrolled factors in measurements

25   that cause normally distributed fluctuations are characterized as random errors and their uncertainties can be reduced by increasing the number of measurements. An example of a random uncertainty in the FPH is the frost control stability. Alternatively, systematic errors remain regardless of the number of measurements, producing biases in the measurements if not corrected. Even if systematic errors are properly understood and corrected there will be a residual error as no correction is perfect. The uncertainty of the mirror temperature measurement by the FPH electronics board is an example of a

30   systematic error. All of the FPH uncertainties are summarized in Table 2.

The largest measurement uncertainties during a sounding arise from instabilities in frost control. The magnitudes of these terms are calculated using the standard error of the estimate of frostpoint temperature over a fixed interval (0.25 km) to determine the residual error from the linear fit (2-σ). The uncertainty is calculated for the balloon ascent and the descent separately. The uncertainty over the 0.25 km interval range is between 0.1 to 1.5 °C in the profile, depending on the

5   instrument performance at any given time.

The mirror temperature uniformity and location of the thermistor embedded in the mirror have been demonstrated to induce systematic uncertainties < 0.1 °C in the CFH frostpoint temperatures (Vömel, 2007a). Uncertainties for the FPH are the same because it uses the same thermistors as the CFH and has mirrors of the same thickness and diameter.

The uncertainty of the mirror temperature measurement on the FPH circuit board varies with the frostpoint temperature due

10   to the ADC. These uncertainties, along with the mirror temperature uniformity and location uncertainties are combined in quadrature to produce the manufacturing uncertainty in each instrument.

Thermistor calibration fit, calibration repeatability, and the reference thermometer uncertainty are combined in quadrature to yield total uncertainty estimates for both the 3-point and 6-point calibration fits. All FPHs since 2014 use the 6-point fit and have a combined calibration uncertainty of 0.03 °C. All prior instruments using the 3-point fit have a combined uncertainty

15   of 0.1 °C before 1990 and 0.07 °C after 1990 and before the 6-point fit.

Two years of FPH data from Boulder, Colorado are analyzed to show the contributions of the various uncertainty estimates in Fig. 5. Panel (a) shows the average in frostpoint temperature [K] with frost control stability uncertainties dominating the total to 15 km with the other two terms contributing more above 15 km to the top of the flight. The mixing ratio uncertainties shown in Fig. 5b include those computed from the manufactures specifications for radiosonde pressure sensor uncertainties

20   in magenta, and the total with and without the pressure sensor uncertainty (black and dashed gray lines, respectively). Manufacturer quoted radiosonde pressure sensor uncertainties are used for the iMet-1-RSB (1070–400 hPa: ± 1.8 hPa / 400–4 hPa: ± 0.5 hPa) and for the Vaisala RS-80 (1080–3 hPa: ± 1.0 hPa) at the 2-σ accuracy limit (Stauffer, 2014). The uncertainties below 15 km are < 12 % due to both atmospheric variability and less stable frost control. In the stratosphere total uncertainties are < 6 % (Fig. 5b).

25   **5 Mirror condensate**

Condensate, either dew or ice, deposits on the mirror when cryogen is added before the flight. Even at mirror temperatures 0 °C to -40 °C, supercooled liquid water may reside on the mirror before homogeneous nucleation will spontaneously freeze the liquid. The uncertain phase of the condensate between 0 °C and -40 °C is inherent to all chilled mirror frostpoint hygrometers (Fujiwara et al., 2003; Vömel et al., 2007a). Correct identification of the condensate phase is important because

30   the vapor pressures above liquid and ice are very different within this temperature range.

The NOAA FPH compares the relative humidity measured by the attached radiosonde to help determine the phase of the condensate on the mirror. Radiosondes measure atmospheric relative humidity with a thin film polymer capacitive sensing surface. This sensor always reports relative humidity with respect to liquid and does not have ambiguity issues like chilled mirror frostpoint hygrometers. Relative humidity profiles are calculated from the FPH mirror temperatures (0 °C to -40 °C)

5 using the different vapor pressure equations for liquid and ice (Fig. 6), then each is compared to the radiosonde's relative humidity profile to identify when the liquid to ice transition occurs on the mirror. When the condensate starts as liquid this transition occurs around -31 °C. The transition is not instantaneous and may exhibit a lag of as much as 2 minutes during some flights. A sharp dip in the frostpoint temperature occurs when the condensate changes to ice, further helping to distinguish the correct transition point.

10 According to Murphy and Koop (2005) metastable forms of ice, such as cubic and amorphous ice, may exist colder than 200 K in the atmosphere. These have a higher vapor pressure than the most stable form, hexagonal ice. At temperatures > 200 K only hexagonal ice is formed on the frostpoint hygrometer mirror. Below the 200 K threshold cubic ice nucleates first; this is estimated to have a vapor pressure 3 % to 11 % greater than hexagonal ice, depending on which enthalpy measurement is used. The cubic ice eventually transforms to hexagonal ice over a period of minutes to days. If the ice on the mirror is cubic

15 instead of hexagonal the frostpoint temperatures must bias warm to compensate for the greater equilibrium vapor pressure above cubic ice. This leads to high biases in the partial pressures calculated from the Goff-Grach equation, and therefore high biases in the water vapor mixing ratios. For this reason, during every balloon ascent when the frostpoint temperature reaches -53 °C, the ice on the mirror is completely sublimed by a heat pulse (mirror clear) followed by rapid frost regrowth within 50 seconds, as is done during each CFH profile (Vömel, 2007a). Hexagonal ice is quickly reformed on the mirror and

20 is maintained for the duration of the flight because transformation into metastable ice is not possible under atmospheric conditions. The mirror clear is performed at -53 °C (220 K) providing a large window to safely grow hexagonal ice instead of cubic ice which can be formed below 200 K. This procedure helps to eliminate ambiguity during a flight. The older analog instruments switched gains around -55 °C instead of -53 °C. It is unlikely that cubic ice or any other metastable form of ice forms on the FPH mirror after the mirror clear.

25 Thornberry et al. (2011) conducted experiments using a laboratory version of the CFH to study the potential interference of gas-phase nitric acid (HNO$_3$) on chilled mirror frostpoint hygrometers. Mixtures of moist air with up to 4 ppbv of HNO$_3$ for 150 minutes presented no detectable change in the measured mirror temperatures, showing it is unlikely that HNO$_3$ can change the frostpoint temperatures significantly during a typical atmospheric sounding.

6 Pressure activated balloon valve system

30 Obtaining uncontaminated water vapor profiles during a slow descent (i.e., no balloon burst) is accomplished using a valve situated in the neck of a balloon. This technology has been utilized on frostpoint hygrometer flights since 1964 when

Mastenbrook (1966) developed a reliable and simple valve system to release helium from the balloon. A fitting on the valve in the neck of an expandable latex balloon was opened at a predetermined pressure. The valve system evolved out of necessity for two main reasons. First, moisture captured on the balloon during ascent in the wet troposphere can contaminate the ascending hygrometer measurements. This contamination is from outgassing of the balloon and flight train in the dry

5   stratosphere and is intermittent because the FPH pendulums in and out of the wake of the balloon. Once the valve opens the balloon ascent slows then starts to descend, and now the FPH leads the flight train with clean uncontaminated air below. Equally important, the valve provides slow and constant descent rates of ~5 m s^{-1} compared to a burst balloon that descends rapidly (> 50 m s^{-1}) in the stratosphere despite the parachute. The parachute is attached in case the valve fails to open or the balloon bursts before the designated pressure has been attained.

10   The current version of the valve system consists of two pieces: a PVC valve and a digital microcontroller circuit board with a calibrated pressure sensor (Kräuchi et al., 2016). The 175 g valve is constructed from PVC pipe with a plastic lid secured with waxed string. Separate battery packs are used to power the electronics board and to cut the waxed string with a heated nichrome wire at the desired pressure. Custom software allows the user to set the cut down pressure and apply a one-point pressure offset determined from a laboratory pressure standard. The overall accuracy of the pressure sensor, after the one-

15   point offset is applied, is ± 1 hPa with 0.01 hPa resolution. For profiles over Boulder, Lauder, and Hilo the valves are set to open at 16.0 hPa, or roughly 28.5 km.

The new version of the valve and electronics has increased the success rate from 76 % to 94 % for all balloon flights between 1991 and 2014 that did not burst before the cut down pressure was achieved. At the same time the new system decreased the valve system weight by 60 % which saves helium.

7 Intercomparisons

7.1 AquaVIT-2

The Karlsruhe Institute of Technology (KIT) operates a large volume (84 m^3) aerosol and cloud simulation chamber (AIDA) with the ability to vary pressure, temperature, and water vapor mixing ratio in a highly controlled fashion. In April 2013 a

25   two-week-long water vapor measurement intercomparison experiment (AquaVIT-2) was performed at the AIDA chamber. AquaVIT-2 built off a previous intercomparison (AquaVIT-1, Fahey et al., 2014) at the AIDA chamber in October 2007 in which the NOAA FPH did not participate. A special laboratory version of the balloon FPH was constructed specifically for AquaVIT-2 to externally measure chamber air extracted through a heated tube by a downstream pump. The laboratory instrument has three main differences from the balloon version. First, liquid nitrogen was used as the cryogen in the

30   laboratory instrument, requiring a Teflon sleeve to partially insulate the copper cold finger from the colder liquid nitrogen.

Next, the sensor housing and intake tubing were modified to connect to the heated extraction tube without any leaks since most of the chamber experiments were done at sub-ambient pressures. Finally, the flowrates through the laboratory instrument were reduced when compared to the balloon sonde to conserve the chamber air.

The purpose of AquaVIT-2 was to intercompare state-of-the-art and prototype atmospheric hygrometers with each other and with independent humidity standards to determine precision and accuracy of the different instruments. Each day the chamber was held at one specific temperature while pressure and water vapor mixing ratio were changed throughout the day. Daily chamber temperatures ranged from 190–233 K over the 10-day experiment (Fig. 7a). Dynamic temperature excursions of nearly ± 10 K caused by adiabatic expansion and compression when air was removed from or added to the chamber, were not included in the analysis. The water vapor mixing ratios varied between ~ 0.15 and 1000 ppmv while the pressure in the chamber started each day between 50–100 hPa and increased stepwise to a maximum of 300–1000 hPa before stepping back down to 80–100 hPa at the end of each day. Typically there were six distinct pressure steps throughout the day to intercompare the instruments during quasi-static conditions. Temperature and pressure in the chamber were stable within ± 0.3 K (1-σ) and ± 0.35 hPa (1-σ), respectively, during each of the 36 measurement segments examined. Three of the 10 experiment days were established as blind intercomparison days when data were sent directly to independent and impartial referees. Here we focus on comparing six of the seven non-blind days between the NOAA FPH and the MC-APicT-1.4, an open-path, in-cloud, direct tunable diode laser absorption spectrometer (dTDLAS) (Kühnreich et al., 2015). MC-APicT-1.4 is a successor of the initial APICT-instrument described in (Ebert et al., 2005) and selectively measures, without any gas sampling process, the interstitial water vapor mixing ratio within the AIDA chamber (even within an ice cloud) with help from an open path white cell integrated into the AIDA chamber. All MC-APicT-1.4 data were evaluated by the German national metrology institute (PTB) based on a proprietary, calibration-free first principles dTDLAS approach. The validity of this data evaluation was recently successfully demonstrated by comparing PTB's extractive, airborne dTDLAS field hygrometer, SEALDH, with the German primary humidity standard at PTB (Buchholz et al., 2014). The three blind days are excluded because the data are still not available.

Temperatures and water vapor mixing ratios during nearly all the static air temperature segments were within the observed range measured by the NOAA FPH in the atmosphere. The exception was experiment 3 on 10 April 2013 (Fig. 7c) which was colder and drier than the real stratosphere. Only a quarter of the water vapor mixing ratios during stable pressure segments were within the range observable by the NOAA FPH (Fig. 7d). A total of 36 stable sections were analyzed, each lasting an average of 28 minutes. Excluding data from experiment 3, the agreement between the FPH and the MC-APicT-1.4 instrument was 1.0 ± 5.5 % (2-σ) for realistic atmospheric conditions between 2 and 600 ppmv. From here forward, the uncertainties presented with mean values are always twice the standard deviation. Below 1.5 ppmv the agreement is better than 30 % (Fig. 8a). Although the 15–30 % differences for experiment 3 appear to be large, the absolute differences are small, ranging from 0.02–0.43 ppmv (Fig. 8b).

The FPH data collected over the non-blind days in the region of interest (0.1 to 10 ppmv) show good agreement with the MC-APicT-1.4 instrument. Even including the six stable sections < 1.5 ppmv where the FPH was measuring 15–30 % higher than MC-APicT-1.4, the linear trend between the two instruments shows a slope of 1.014 and near-zero y-intercept with minimal scatter as seen in Fig. 9.

7.2 Dual frostpoint hygrometer balloon flights

To exclude the atmospheric variability and pressure measurement uncertainty, two FPHs were flown using a single balloon and radiosonde on 08 November 2011. The mean differences in frostpoint temperature and water vapor mixing ratio (0.25 km bin averages) between the two hygrometers were -0.019 ± 0.25 °C and -0.16 ± 3.9 %, respectively (Fig. 10).

Similarly, a dual flight with a CFH and an FPH using a single radiosonde and balloon was flown in Boulder, Colorado on 13 April 2015. The agreement was 0.35 ± 10 % as seen in Fig. 11 even when taking into account the differences larger than 10 % that occurred when the mixing ratio was changing quickly. The FPH dual flight data (Fig. 10) were plotted as frostpoint temperature differences to show the full range of the data. The CFH FPH dual flight data are plotted as mixing ratio differences to show their full range.

8.0 Summary

Since 1980 the NOAA FPH has acquired high quality monthly vertical profiles of water vapor over Boulder, CO. The instrument has evolved over the years but the physical measurement principal and the calibration process has not deviated, making the stability of FPH measurement accuracy suitable for long-term monitoring and process studies. In 2004, a second FPH sounding site was added at Lauder, New Zealand, initiating what is now the longest upper-atmospheric water vapor record in the Southern Hemisphere. A third site at Hilo, Hawaii was started late in 2010 to measure tropical water vapor profiles, complementing the measurement programs at the existing northern and southern mid-latitude locations.

Improvements to the microcontroller version of the instrument in 2008 lead to more high quality flights at the three NOAA/GMD water vapor sites. The biggest improvements to the FPH were implementing digital sunlight filtering to eliminate the sunshield, adding a lens heater, and creating a frostpoint dependent gain schedule.

The various contributions to the uncertainty of the instrument are calculated for each profile. The overall uncertainty in the stratosphere is typically < 6 % increasing to < 12 % in the troposphere. The majority of the uncertainty estimate resides in the frost control stability during a flight.

In 2014 a new continuous mirror thermistor calibration technique was adopted. This allows a 6-point calibration fit that reduces fit errors to ± 0.01 °C compared to ± 0.06 °C for the older 3-point method. A lag correction was also developed to account for the larger PRT thermometer having a slower response time than the tiny FPH thermistors. This correction was determined by comparing the results from the old and new calibration techniques for the same batch of 39 thermistors.

5   Comparison data during the AquaVIT-2 chamber experiment in Karlsruhe, Germany with the MC-APicT-1.4 direct tunable diode laser spectrometer show good agreement over six non-blind days of experiments. For water vapor mixing ratios between 2 and 600 ppmv the agreement was 1.0 % ± 5.5 %. Dual FPH/FPH and FPH/CFH balloon flights show excellent consistency between instruments and do not give any indication of a bias.

Acknowledgments

10   The authors would like to thank Frank Polacek III, Ron Thorne, Michael O'Neill, David "Zim" Sherman, Patrick Cullis, Hamish Chrisholm, Alan Thomas, David Nardini, Darryl Kuniyuki, Wills Dobson, Richard Querel, and all of the other people who have helped build and launch water vapor sondes since the program started in 1980. We thank the US GCOS Program for continued funding support for Lauder, New Zealand and the NOAA climate program office for support with operation costs at Hilo, Hawaii. Support from the NASA Upper Atmospheric Research Program provides imperative funding

15   to all three NOAA/GMD sites. The AquaVIT-2 experiment was partially supported by the EMRP project METEOMET (ENV07) and FP7 project EUROCHAMP2. The EMRP is jointly funded by the EMRP participating countries within EURAMET and the European Union. The authors thank Chance Sterling for helpful conversation and comments on this manuscript.

20   **References**

Brewer, A. W.: Evidence for a world circulation provided by the measurements of helium and water vapor distribution in the stratosphere. Quart. J. Roy. Meteor. Soc., 75, 351–363, 1949.

Buchholz, B., Böse, N., Ebert, V.: Absolute validation of a diode laser hygrometer via intercomparison with the German national primary water vapor standard, App Physics B, 116(4), 883-899, doi:10.1007/s00340-014-5775-4, 2014.

25   Clark, L. E.: Report of the determination of exactness of fit of thermistor to the equations logR=A+B/(T+2) and logR=A+B/(T+2)+CT, Tech. Rep. 2168, U.S. Army Signal Res. and Dev. Lab, 1961.

Ebert, V., Teichert, H., Giesemann, C., Saathoff, H., & Schurath, U.: Fibre-Coupled In-situ Laser Absorption Spectrometer for the Selective Detection of Water Vapour Traces down to the ppb-Level. Tm - Technisches Messen, 72(1-2005), 23–30. http://doi.org/10.1524/teme.72.1.23.56689, 2005.

30   Fahey, D. W., Gao, R.-S., Möhler, O., Saathoff, H., Schiller, C., Ebert, V., Krämer, M., Peter, T., Amarouche, N., Avallone, L. M., Bauer, R., Bozóki, Z., Christensen, L. E., Davis, S. M., Durry, G., Dyroff, C., Herman, R. L., Hunsmann, S., Khaykin, S. M., Mackrodt, P., Meyer, J., Smith, J. B., Spelten, N., Troy, R. F., Vömel, H., Wagner, S., and Wienhold, F. G.: The

AquaVIT-1 intercomparison of atmospheric water vapor measurement techniques, Atmos. Meas. Tech., 7, 3177-3213, doi:10.5194/amt-7-3177-2014, 2014.

Forster, P. M. de F., and Shine, K. P.: Assessing the climate impact of trends in stratospheric water vapor, Geophys. Res. Lett., 29(6), 1086, doi:10.1029/2001GL013909, 2002.

5 Fujiwara, M., M. Shiotani, F. Hasebe, H. Vömel, S. J. Oltmans, P. W. Ruppert, T. Horinouchi, and T. Tsuda: Performance of the Meteolabor "SnowWhite" chilled mirror hygrometer in the tropical troposphere: Comparisons with the Vaisala RS-80 A/H humicap sensors, J. Atmos. Oceanic Technol, 20, 1534-1542, 2003.

Goff, J. A., and Gratch, S.: Low-pressure properties of water from -160 to 212 F, Trans. Am. Soc. Heating Ventilating Eng., 52, 95–122, 1946.

10 Goff, J. A.: Saturation pressure of water on the new Kelvin temperature scale, Trans. Am. Heat. Ventilat. Engineers, 63, 347-354, 1957.

Hurst, D. F., Oltmans, S. J., Vömel, H., Rosenlof, K. H., Davis, S. M., Ray, E. A., Hall, E. G., and Jordan, A. F.: Stratospheric water vapor trends over Boulder, Colorado: Analysis of the 30 year Boulder record, J. Geophys. Res., 116, D02306, doi:10.1029/2010JD015065, 2011a.

15 Hurst, D. F., Hall, E. G., Jordan, A. F., Miloshevich, L. M., Whiteman, D. N., Leblanc, T., Walsh, D., Vömel, H., and Oltmans, S. J.: Comparisons of temperature, pressure and humidity measurements by balloon-borne radiosondes and frost point hygrometers during MOHAVE-2009, Atmos. Meas. Tech., 4, 2777-2793, doi:10.5194/amt-4-2777-2011, 2011b.

Hurst, D. F., Lambert, A., Read, W. G., Davis, S. M., Rosenlof, K. H., Hall, E. G., Jordan, A. F., Oltmans, S. J.: Validation of Aura Microwave Limb Sounder stratospheric water vapor measurement by the NOAA frost point hygrometer, J. Geophys.

20 Res. Atmos., 119, 1612-1625, doi:10.1002/2013JD020757, 2014.

JCGM/WG 1: Evaluation of measurement data – Guide to the expression of uncertainty in measurement, International Bureau of Weights and Measures / Bureau International des Poids et Mesures, http://www.bipm.org/utils/common/documents/jcgm/JCGM_100_2008_E.pdf (last access: September 2015), 2008.

Kley, D., Russell III, J. M., and Philips, C.: SPARC Assessment of Upper Tropospheric and Stratospheric Water Vapour,

25 World Meteorol. Org., Geneva, 2000.

Kräuchi, A., R. Philipona, G. Romanens, D.F. Hurst, E.G. Hall, and A.F. Jordan, Controlled weather balloon ascents and descents for atmospheric research and climate monitoring, Atmos. Meas. Tech., 9, 929–938, doi:10.5194/amt-9-929-2016, 12559-12588, 2016

Kühnreich, B., Wagner, S., Habig, J. C., Möhler, O., Saathoff, H., & Ebert, V.: Time-multiplexed open-path TDLAS

30 spectrometer for dynamic, sampling-free, interstitial $H_2^{18}O$ and $H_2^{16}O$ vapor detection in ice clouds. Applied Physics B, 119(1), 177–187. http://doi.org/10.1007/s00340-015-6074-4, 2015.

Lambert, A., Read, W. G., Livesey, N. J., Santee, M. L., Manney, G. L., Froidevaux, L., Wu, D. L., Schwartz, M. J., Pumphrey, H. C., Jimenez, C., Nedoluha, G. E., Cofield, R. E., Cuddy, D. T., Daffer, W. H., Drouin, B. J., Fuller, R. A., Jarnot, R. F., Knosp, B. W., Pickett, H. M., Perun, V. S., Snyder, W. V., Stek, P. C., Thurstans, R. P., Wagner, P. A., Waters,

J. W., Jucks, K. W., Toon, G. C., Stachnik, R. A., Bernath, P. F., Boone, C. D., Walker, K. A., Urban, J., Murtagh, D., Elkins, J. W., Atlas, E.: Validation of the Aura Microwave Limb Sounder middle atmosphere water vapor and nitrous oxide measurements, J. Geophys. Res., 112, D24S36, doi:10.1029/2007JD008724, 2007.

Lee, J., Yang, P., Dessler, A. E., Gao, B.–C., and Platnick, S.: Distribution and radiative forcing of tropical thin cirrus clouds, J. Atmos. Sci., 66(12), 3721–3731, doi:10.1175/2009jas3183.1, 2009.

Mastenbrook, H. J., and Dinger, J. E.: Distribution of Water Vapor in the Stratosphere, J. Geophys. Res., 66, 1437-1444, 1961.

Mastenbrook, H. J.: A control system for ascent-descent soundings of the atmosphere, J. Applied Meteorology, 5, 737-740, 1966.

Mastenbrook, H. J.: Operation Manual for Model 1012 Hygrometer, Naval Research Laboratory Instruction Book, 176, 1981.

Mastenbrook, H. J., and Oltmans, S. J.: Stratospheric water vapor variability for Washington, DC/Boulder, CO: 1964–82, J. Atmos. Sci., 40, 2157–2165, 1983.

Mote, P. W., Rosenlof, K. H., McIntyre, M. E., Carr, E. S., Gille, J. C., Holton, J. R., Kinnersley, J. S., Pumphrey, H. C., Russell III, J. M., and Waters, J. W.: An atmospheric tape recorder: The imprint of tropical tropopause temperatures on stratospheric water vapor, J. Geophys. Res., 101(D2), 3989–4006, doi:10.1029/95JD03422, 1996.

Murphy, D. M., and Koop, T.: Review of the vapour pressures of ice and supercooled water for atmospheric applications, Q. J. R. Meteorol. Soc., 131, 1539–1565, 2005.

Oltmans, S. J.: Measurements of water vapor in the stratosphere with a frost-point hygrometer, Moisture and Humidity-1985-Measurement and Control in Science and Industry, 251-258, 1985.

Oltmans, S. J., and Hofmann, D. J.: Increase in lower-stratospheric water vapour at a mid-latitude northern hemisphere site from 1981 to 1994, Nature, 374, 146–149, doi:10.1038/374146a0, 1995.

Oltmans, S. J., Vömel, H., Hofmann, D. J., Rosenlof, K. H., and Kley, D.: The increase in stratospheric water vapor from balloonborne, frostpoint hygrometer measurements at Washington, D.C., and Boulder, Colorado, Geophys. Res. Lett., 27(21), 3453–3456, doi:10.1029/2000GL012133, 2000.

Randel, W. J., Wu, F., Vömel, H. Nedoluha, G. E., and Foster, P.: Forster, Decreases in stratospheric water vapor after 2001: Links to changes in the tropical tropopause and the Brewer-Dobson circulation, J. Geophys. Res., 111, D12312,doi:10.1029/2005JD006744, 2006.

Read, W. G., Lambert, A., Bacmeister, J., Cofield, R. E., Christensen, L. E., Cuddy, D. T., Daffer, W. H., Drouin, B. J., Fetzer, E., Froidevaux, L., Fuller, R., Herman, R., Jarnot, R. F., Jiang, J. H., Jiang, Y. B., Kelly, K., Knosp, B. W., Kovalenko, L. J., Livesey, N. J., Liu, H.-C., Manney, G. L., Pickett, H. M., Pumphrey, H. C., Rosenlof, K. H., Sabounchi, X., Santee, M. L., Schwartz, M. J., Snyder, W. V., Stek, P. C., Su, H., Takacs, L. L., Thurstans, R. P., V̈omel, H., Wagner, P. A., Waters, J. W., Webster, C. R., Weinstock, E. M., and Wu, D. L.: Aura Microwave Limb Sounder upper tropospheric

and lower stratospheric H2O and relative humidity with respect to ice validation, J. Geophys. Res., 112, D24S35, doi:10.1029/2007JD008752, 2007.

Rohs, S., C. Schiller, M. Riese, A. Engel, U. Schmidt, T. Wetter, I. Levin, T. Nakazawa, and S. Aoki: Long-term changes of methane and hydrogen in the stratosphere in the period 1978–2003 and their impact on the abundance of stratospheric water vapor, J. Geophys. Res., 111, D14315, doi:10.1029/2005JD006877, 2006.

Rollins, A. W., Thornberry, T. D., Gao, R. S., Smith, J. B., Sayres, D. S., Sargent, M. R., Schiller, C., Krämer, M., Spelten, N., Hurst, D. F., Jordan, A. F., Hall, E. G., Vömel, H., Diskin, G. S., Podolske, J. R., Christensen, L. E., Rosenlof, K. H., Jensen, E. J., Fahey, D. W.: Evaluation of UT/LS hygrometer accuracy by intercomparison during the NASA MACPEX mission, J. Geophys. Res. Atmos., 119, 1915–1935, doi:10.1002/2013JD020817, 2014.

Rosenlof, K. H., and Reid, G. C.: Trends in the temperature and water vapor content of the tropical lower stratosphere: Sea surface connection, J. Geophys. Res., 113, D06107, doi:10.1029/2007JD009109, 2008.

Scherer, M., Vömel, H., Fueglistaler, S., Oltmans, S. J., and Staehelin, J.: Trends and variability of midlatitude stratospheric water vapour deduced from the re-evaluated Boulder balloon series and HALOE, Atmos. Chem. Phys., 8, 1391–1402, doi:10.5194/acp-8-1391-2008, 2008.

Solomon, S., Rosenlof, K. H., Portmann, R. W., Daniel, J. S., Davis, S. M., Sanford, T. J., and Plattner, G.-K.: Contributions of stratospheric water vapor to decadal changes in the rate of global warming, Science, 327, 1219–1223, doi:10.1126/science.1182488, 2010.

Stauffer, R. M., Morris, G. A., Thompson, A. M., Joseph, E., Coetzee, G. J. R., and Nalli, N. R.: Propagation of radiosonde pressure sensor errors to ozonesonde measurements, Atmos. Meas. Tech., 7, 65–79, doi:10.5194/amt-7-65-2014, 2014.

Steinhart, I. S., and Hart, R.: Calibration curves for thermistors, Deep Sea Res., 15, 497-503, 1968.

Thornberry, T., Gierczak, T., Gao, R. S., Vömel, H., Watts, L. A., Burkholder, J. B., and Fahey, D. W.: Laboratory evaluation of the effect of nitric acid uptake on frost point hygrometer performance, Atmos. Meas. Tech., 4, 289-296, doi:10.5194/amt-4-289-2011, 2011.

Vömel, H., Oltmans, S. J., Hofmann, D. J., Deshler, T., and Rosen, J. M.: The evolution of the dehydration in the Antarctic stratospheric vortex, J. Geophys. Res., 100, 13,919–13,926, 1995.

Vömel, H., David, D. E., and Smith, K.: Accuracy of tropospheric and stratospheric water vapor measurements by the cryogenic frost point hygrometer: Instrumental details and observations, J. Geophys. Res., 112, 8305, doi:10.1029/2006JD007224, 2007a.

Vömel, H., Yushkov, V., Khaykin, S., Korshunov, L., Kyro, E., and Kivi, R.: Intercomparison of stratospheric water vapor sensors: FLASH-b and NOAA/CMDL frost point hygrometer, J. Atmos. Ocean. Tech., 27, 941–952, doi:10.1175/JTECH2007.1, 2007b.

Vömel, H., Barnes, J. E., Forno, R. N., Fujiwara, M., Hasebe, F., Iwasaki, S., Kivi, R., Komala, N., Kyrö, E., Leblanc, T., Morel, B., Ogino, S.-Y., Read, W. G., Ryan, S. C., Saraspriya, S., Selkirk, H., Shiotani, M., Valverde Canossa, J.,

Whiteman, D. N.: Validation of Aura Microwave Limb Sounder water vapor by balloon-borne Cryogenic Frost point Hygrometer measurements, J. Geophys. Res., 112, D24S37, doi:10.1029/2007JD008698, 2007c.

Weinstock, E. M., Smith, J. B., Sayres, D. S., Pittman, J. V., Spackman, J. R., Hintsa, E. J., Hanisco, T. F., Moyer, E. J., St. Clair, J. M., Sargent, M. R., and Anderson, J. G.: Validation of the Harvard Lyman- in situ water vapor instrument:
5 Implications for the mechanisms that control stratospheric water vapor, J. Geophys. Res., 114, D23301, doi:10.1029/2009JD012427, 2009.

Table 1: The four versions of the NOAA FPH flown between the present day and 1980 along with the radiosondes, weights, and data acquisition method.

FPH Version	Period	Radiosonde Frequency and Model	Data Acquisition Method	Weight without cryogen (g)
FPH V1	1980-1991	1680 MHz VIZ "A"	Analog Strip chart recorder	1550
FPH V2	1991-2004	403 MHz Vaisala RS-80	Digital Strato software	1500
FPH V3	2004-2008	403 MHz Vaisala RS-80	Digital Strato software	475
FPH V4	2008-present	403 MHz InterMet iMet-1-RSB	Digital SkySonde Client/Server	450

Table 2: Overview of the sources contributing to the FPH uncertainty budget. Combining the frost stability, manufacturing variability, and thermistor calibration uncertainties in quadrature can be calculated for a fixed interval in the FPH profile.

Uncertainty Parameter	Value	Random or Systematic
Frost control stability, u_Frost_Control	0.1 to 1.5 K	R
Temperature uniformity of the mirror, u_Mirror_Uniform	< 0.1 K	S
FPH electronics board thermistor measurement, u_FPH_ADC	< 0.02 K (stratosphere), < 0.17 K (troposphere)	S, *
Manufacturing uncertainty total, u_Manuf	$= (u\_Mirror\_Uniform^2 + u\_FPH\_ADC^2)^{1/2}$	S, *
Thermistor calibration fit, u_Cal_Fit	0.06 K (3-point fit), 0.01 K (6-point fit)	S
Thermistor calibration repeatability, u_Cal_Repeat	0.043 K (3-point fit), 0.028 K (6-point fit)	S
Reference thermometer, u_Ref_Therm	0.01 K after 1998, 0.075 K before 1998	S

Thermistor calibration total, u_Therm_Cal	$= (u\_Cal\_Fit^2 + u\_Cal\_Repeat^2 + u\_Ref\_Therm^2)^{1/2}$, S, ** 0.1 K < 1990, 0.07 K > 1990 (3-point fit), 0.03 K (6-point fit)
NOAA FPH uncertainty total, u_FPH	$= (u\_Frost\_Control^2 + u\_Manuf^2 + u\_Therm\_Cal^2)^{1/2}$

*, dependent on frostpoint temperature

**, constant in profile
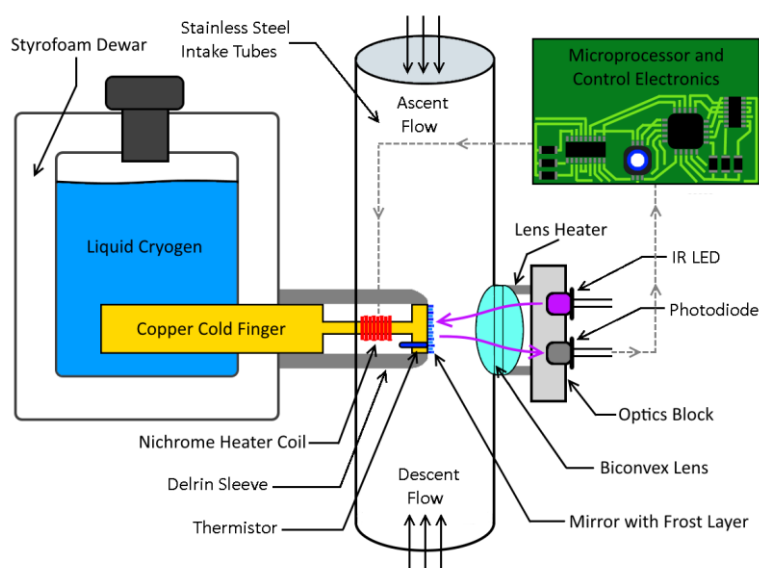
Figure 1: Schematic of the NOAA FPH instrument. The electronics board and optics block are enclosed by insulating foam along with the battery pack while the lens, intake tubes, and mirror head are all exposed to ambient air. The microcontroller uses the photodiode signal to regulate the mirror temperature such that the reflectivity of the frost on the mirror is constant over the flight.
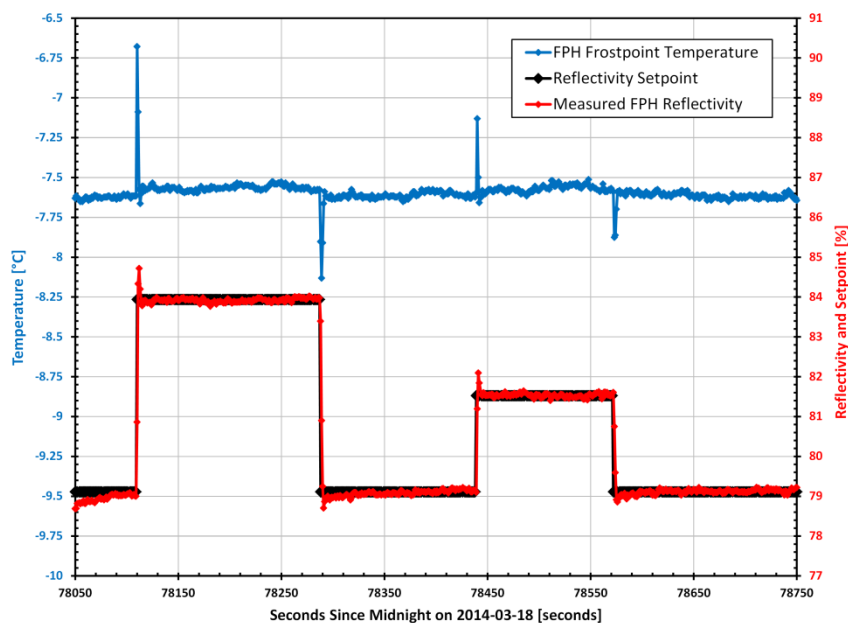
Figure 2: The frostpoint temperature measured by the NOAA FPH mirror thermistor (blue) remains unchanged when varying the amount of condensate on the mirror by adjusting the reflectivity setpoint (black). The measured reflectivity of the mirror is shown in red. Ambient laboratory air was sampled during this experiment.
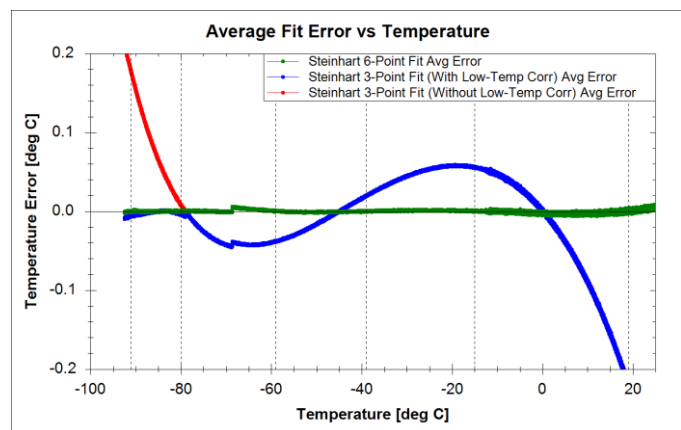
Figure 3: Difference between two different calibration fits and the actual measured bath temperature during a calibration run. Each curve is comprised of the mean of 39 thermistors fit errors. The Steinhart-Hart 3-point fit is shown with (blue) and without (red) the low temperature correction. All flights between 1980 and 2013 utilize the 3-point fit with the low temperature correction. Flights starting in
10   2014 do not need a low temperature correction since the new 6-point thermistor fit (green) was implemented. Dashed lines show the six calibration points.
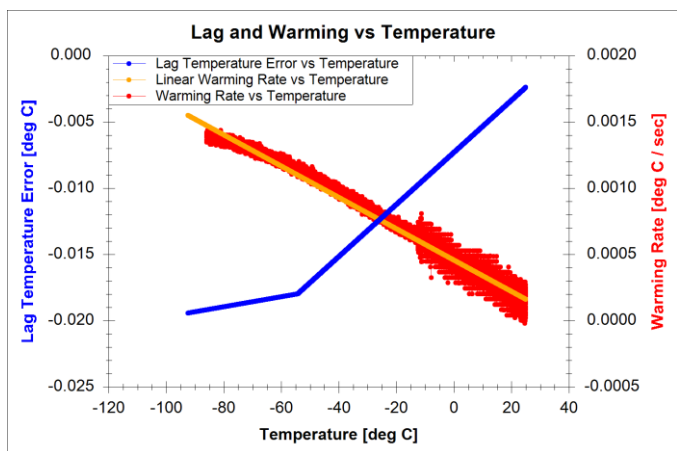
Figure 4: Temperature correction applied to raw NIST-traceable PRT thermometer readings to account for the lag between the larger PRT thermometer and the small thermistors in the alcohol bath.
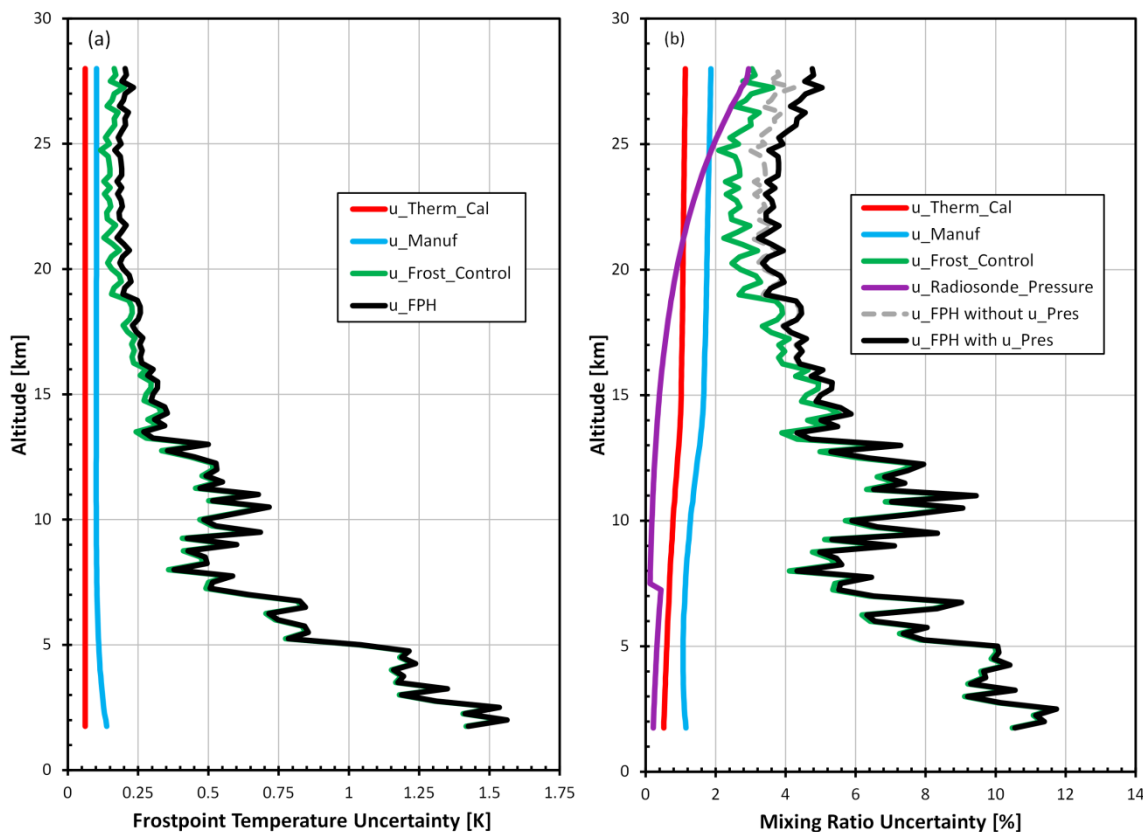
Figure 5: Contributions of specific uncertainty terms to the total FPH uncertainties in frostpoint temperature (a) and water vapor mixing ratio (b). The FPH uncertainties shown are the mean values from 24 flights in Boulder, CO. Radiosonde pressure uncertainties (magenta) are based on InterMet's sensor specifications that decrease at 8 km, producing the discontinuity.
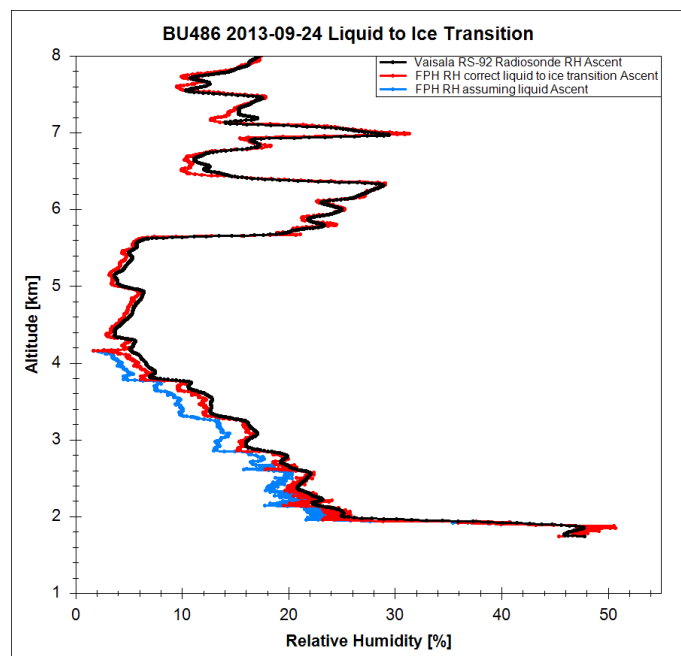
Figure 6: The liquid to ice transition on the FPH mirror can be seen at 4.2 km on the ascent. Using the appropriate vapor pressure formulations below and above the point of condensate transition brings the RH values of the FPH and the Vaisala RS-92 into agreement.
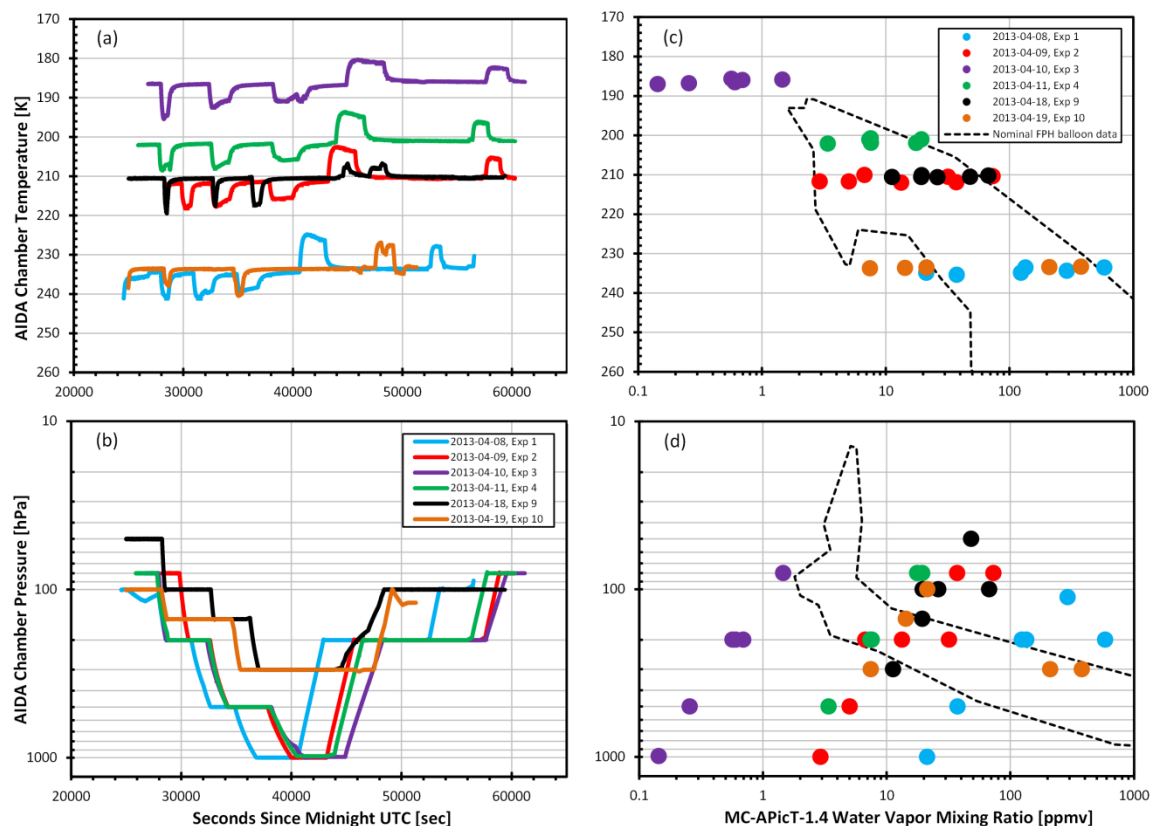
Figure 7: Daily time series of temperatures (a), and pressures (b), for all data during the six non-blind experiments are shown. The relationship between chamber temperature and pressure with 36 individual stable water vapor mixing ratio segments are shown in panels c and d, respectively. Areas contained by dashed lines indicate the range of water vapor and temperature in the actual atmosphere.
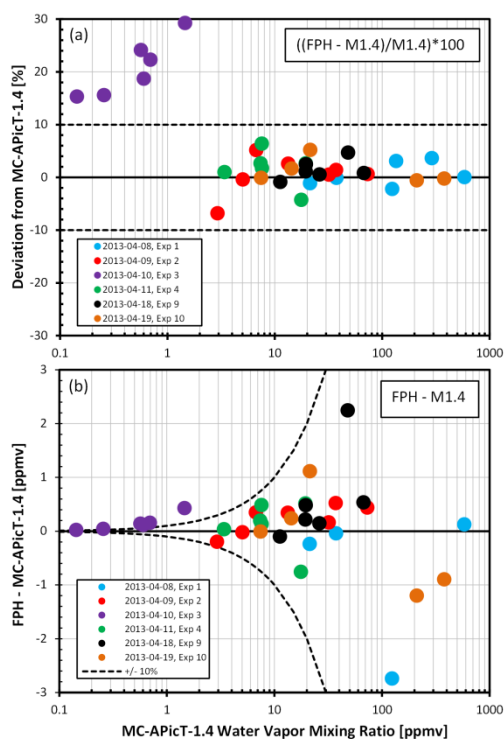
Figure 8: Difference between NOAA FPH and MC-APicT-1.4 mixing ratios in (a) relative % and (b) absolute (ppmv) units for mixing ratios between 0.1 and 600 ppmv over the six days of non-blind experiments.
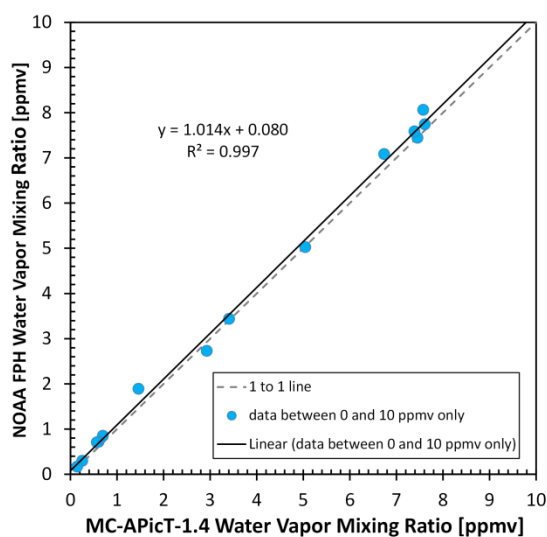
Figure 9: Correlation plot showing all data collected between 0.1 and 10 ppmv over the six static non-blind days of experiments. A linear trend line (black) is shown with slope and offset.
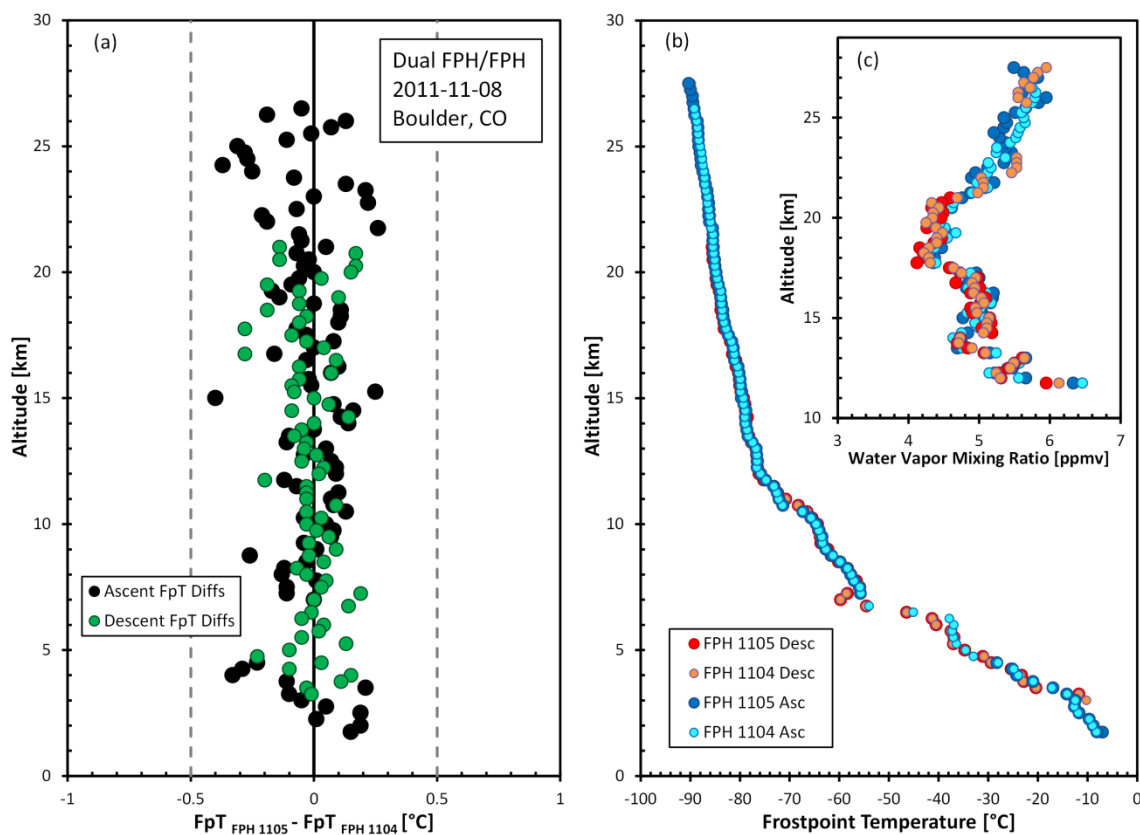
Figure 10: Frostpoint temperature differences from a dual FPH flight on the same balloon in Boulder, CO are shown for the ascent (black) and descent (green). The frostpoint profiles (b) along with the stratospheric water vapor mixing ratios between 3 and 7 ppmv (c) show
5   agreement over the entire flight.
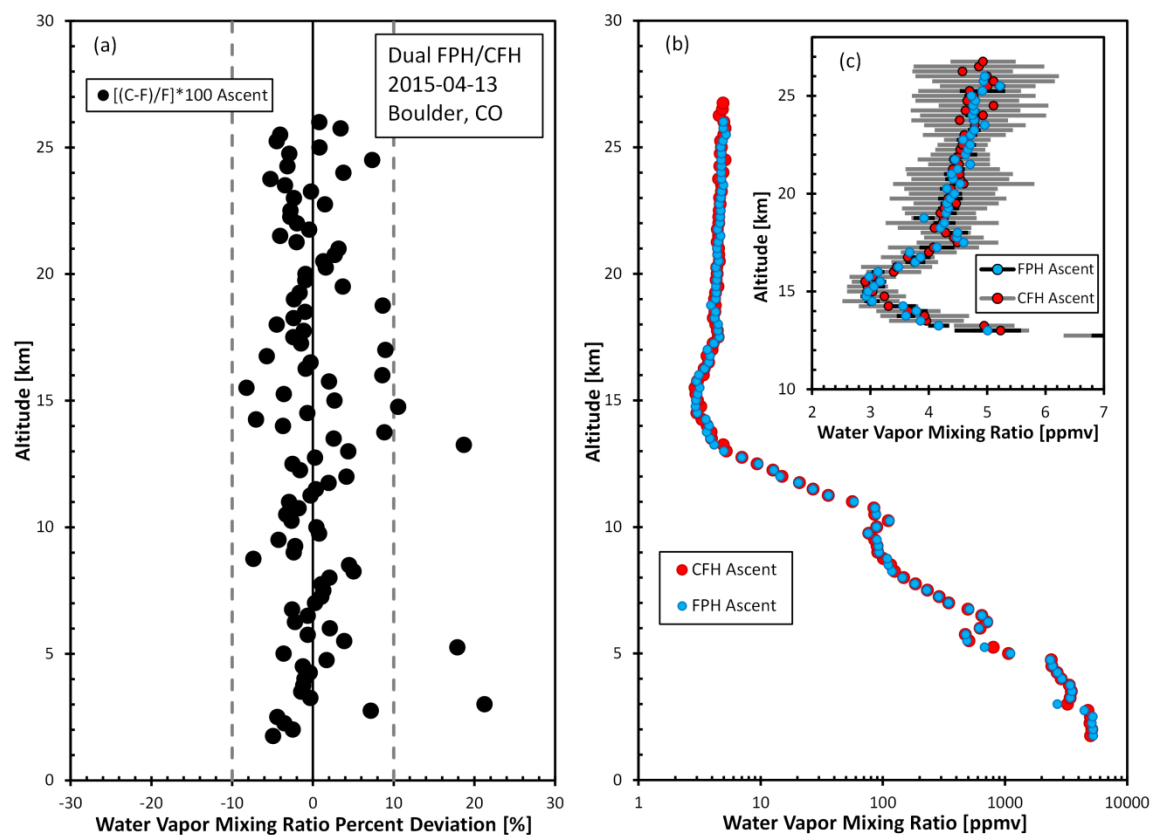
Figure 11: Mixing ratio deviations are shown between the CFH and FPH (a) beside the full stratospheric water vapor mixing ratio plot (b). Stratospheric water vapor mixing ratios between 2 and 7 ppmv are show in panel (c) where the error bars are ± 1-σ for the 0.25 km bins in gray (CFH) and black (FPH).